GEUS Bulletin

RESEARCH ARTICLE

P–T conditions of anthophyllite- and garnet-bearing metapelites of the Nunatarsuaq domain, Nagssugtoqidian orogen, West Greenland

Valdemar O. Enevoldsen[1]*, Thomas F. Kokfelt[2], Andrew J. Locock[3], Trine Ravn-Jonsen[1], Kristine Thrane[2], Tod E. Waight[4], James M. Scott[1]

[1]Department of Geoscience, Aarhus University, Aarhus, Denmark; [2]Department of Mapping and Mineral Resources, Geological Survey of Denmark and Greenland, Copenhagen, Denmark; [3]Department of Earth and Atmospheric Sciences, University of Alberta, Edmonton, Canada; [4]Department of Geosciences and Natural Resource Management (Geology Section), University of Copenhagen, Copenhagen K, Denmark

Abstract

Anthophyllite- and garnet-bearing metapelites from the Nunatarsuaq domain, located north of the UNESCO World Heritage site Ilulissat Icefjord (Kangiata Sullua) in Greenland at the northern margin of the Nagssugtoqidian orogen, enable a first quantitative assessment of the conditions of metamorphism in the area. Geothermobarometry undertaken on metapelites from a representative section of the domain indicates peak metamorphic conditions of *c.* 700–750°C and *c.* 8–9.5 kbar implying burial to mid–lower-crustal depths during deformation. The high-temperature range is consistent with the occurrence of widespread textural evidence for partial melting in the rocks. Retrograde chlorite, epidote and actinolite along with reverse zoning of Mn in garnet rims record subsequent cooling and hydration during exhumation into lower amphibolite to greenschist facies conditions, although the timing is unclear. The recognition of upper-amphibolite facies metamorphic conditions indicates that the Nunatarsuaq domain likely shared a common Palaeoproterozoic 1.82–1.81 Ga metamorphic event, probably associated with crustal thickening during collision of the Rae and North Atlantic cratons in the Nagssugtoqidian orogen. These findings reveal that the Nunatarsuaq domain preserves a higher-grade metamorphic imprint than previously recognised and refine the metamorphic architecture of the northern Nagssugtoqidian orogen.

1 Introduction

The Archaean North Atlantic and Rae cratons in West Greenland were assembled during the Palaeoproterozoic (*c.* 1.9–1.7 Ga) into the Nagssugtoqidian orogen and the Rinkian fold belt (Fig. 1a; Connelly *et al.* 2006). The metamorphic conditions accompanying juxtaposition of these terranes appear to have reached granulite facies in places (Davidson 1979; Connelly *et al.* 2000; Guarnieri *et al.* 2023), with controversial evidence for ultra-high-pressure metamorphism documented from one location (Glassley *et al.* 2014; Schönig *et al.* 2023). Large portions of the orogen display amphibolite facies mineral assemblages (Mazur *et al.* 2012), although there has been limited quantitative assessment of the metamorphic conditions.

The northernmost part of the Nagssugtoqidian orogen in the Nunatarsuaq domain, where our study was conducted, has previously been described as showing amphibolite facies mineral assemblages, but the *P–T* conditions have not been determined (Garde & Steenfelt 1999). The nearest comparable studied area lies approximately 60 km to the south-west, on the Kangilinaaq peninsula, and has been interpreted as lower amphibolite facies (Fig. 1a; Hollis *et al.* 2006). However, within the broader Nagssugtoqidian orogen, the geographically closest rocks with quantitative pressure and temperature estimations (520–550°C, 2.6–3.0 kbar) are staurolite schists

***Correspondence:** *voe@geo.au.dk*
Received: 09 Dec 2025
Revised: 22 May 2026
Accepted: 07 July 2026
Published: 17 Aug 2026

Keywords: amphibolite facies; anthophyllite; Greenland; Nagssugtoqidian; *P–T* conditions

Abbreviations:
GEUS: Geological Survey of Denmark and Greenland
SEM: scanning electron microscope
EDS: Energy Dispersive Spectroscopy
EPMA: Electron probe microanalysis
WDS: wavelength dispersive spectrometry
GBPQ: garnet–biotite–plagioclase–quartz

Edited by: Maja B Rasmussen (University of Copenhagen, Denmark)

Reviewed by: Adam Garde (GEUS, Denmark), Tomas Naeraa (Lund University, Sweden), Sampriti Basak (The Natural History Museum, Denmark)

Funding: See page 14

Competing interests: See page 14

Additional files: See page 14

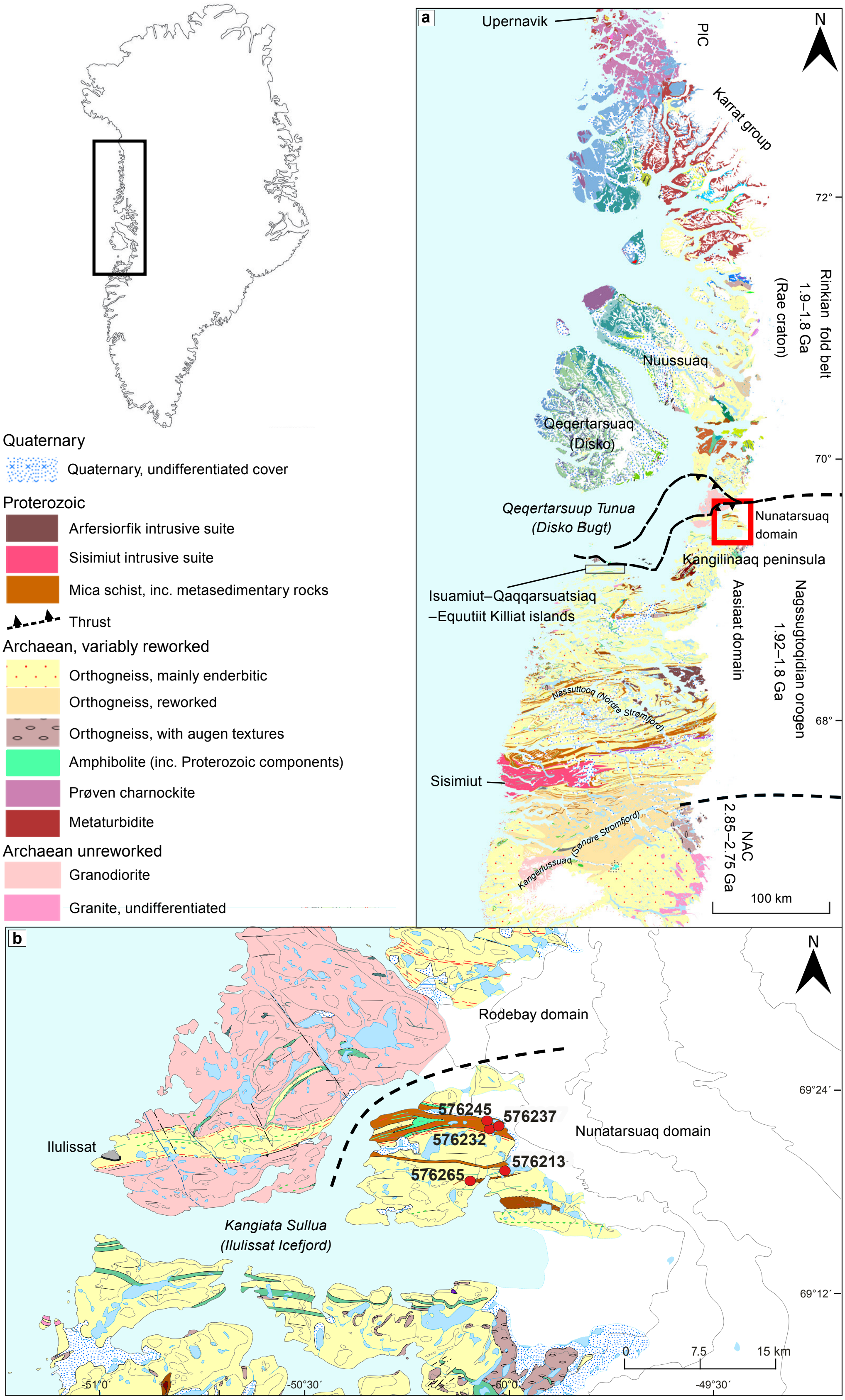

Fig. 1 Geological overview of the study area. See Kokfelt *et al*. (2023) for full legend to base map. (**a**) Regional 1:500 000 scale geological map of Central West Greenland (Garde & Hollis 2010; Kokfelt *et al*. 2023) highlighting the Nunatarsuaq domain. **NAC**: North Atlantic craton; **PIC**: Prøven igneous complex (Garde & Hollis 2010). Subdivisions of orogenic suites are as follows: southern and central Nagssugtoqidian orogen (Connelly *et al*. 2000; Korstgård *et al*. 2006; Mazur *et al*. 2006), northern Nagssugtoqidian orogen (Garde & Hollis 2010; Mazur *et al.* 2012), northern Disko Bugt area (Connelly *et al*. 2006), southern Karrat group (Guarnieri *et al.* 2023), PIC (Dziggel *et al*. 2025). (**b**) Local geological map of the Nunatarsuaq domain showing sample sites (Kokfelt 2024) and *P*–*T* estimates from this study.

located approximately 100 km to the south-west of the Nunatarsuaq domain (Garde & Hollis 2010). Most other work has focused on the predominantly granulite facies central region of the orogen (Davidson 1979; Korstgård *et al.* 2006; Mazur *et al.* 2012). The Nunatarsuaq domain remains a poorly understood segment of the orogen.

Here, we study the metamorphic conditions of a suite of rocks from the Nunatarsuaq domain collected by the Geological Survey of Denmark and Greenland (GEUS) from the Ilulissat Icefjord region during the 2024 field season (Fig. 1b). A sub-suite of garnet-bearing samples has been studied by microbeam methods to obtain high-resolution images of the minerals and their textures and to acquire compositional chemical data to estimate peak metamorphic conditions, thus placing important *P–T* conditions on this part of the orogen.

1.1 Geological setting

The Nagssugtoqidian orogen extends from Kangerlussuaq (Søndre Strømfjord) in the south to Qeqertarsuup Tunua (Disko Bugt) in the north (Fig 1a–b). The orogen is dominated by Archaean orthogneiss with ages of 2.85–2.75 Ga, intercalated with Archaean and Palaeoproterozoic metasediments, as well as Palaeoproterozoic calc-alkaline tonalitic to granodioritic intrusive rocks representing a precollisional magmatic arc (Connelly *et al.* 2006). Throughout most of the orogen, Archaean gneissic fabrics are overprinted by Palaeoproterozoic deformation, with granulite facies metamorphism in the centre of the orogen representing its maximum metamorphic grade (van Gool *et al.* 2002).

The Rinkian fold belt extends from Qeqertarsuup Tunua to *c*. 200 km north of Upernavik (Fig. 1a). The fold belt is underlain by Archaean orthogneiss correlated to the Rae Craton. This basement is unconformably overlain by a thick sequence of metasediments of the Palaeoproterozoic Karrat Group, which were metamorphosed at *c*. 1.9–1.8 Ga (Connelly *et al.* 2006; Sanborn-Barrie *et al*. 2017; Thrane 2021). Based on the distribution of Palaeoproterozoic rocks, the main suture between the Rae and North Atlantic cratons is proposed to lie within the central Qeqertarsuup Tunua area (Fig. 1a; Connelly *et al.* 2006). Once thought to represent two different orogenic belts separated by a low metamorphic grade zone in the Qeqertarsuup Tunua area, the Nagssugtoqidian orogen and Rinkian fold belt have been re-interpreted to reflect a more than 1100 km wide asymmetric orogen (Connelly & Thrane 2005).

The most recent plate tectonic model for the Nagssugtoqidian orogen suggests two S-, to SSE-dipping subduction zones separated by the Archaean Aasiaat domain (Garde & Hollis 2010). The northern suture in the Qeqertarsuup Tunua area forms a network of thrust faults related to early collision between the Rae craton and Aasiaat domain. The Qeqertarsuup Tunua area north of the UNESCO World Heritage site Ilulissat Icefjord (Kangiata Sullua) is divided into four tectonostratigraphic domains, the Nuussuaq, Ataa, Rodebay and Nunatarsuaq domains, dominated by Archaean orthogneiss intercalated or overlain by Archaean and Palaeoproterozoic supracrustal belts (Garde & Steenfelt 1999).

The southernmost domain, Nunatarsuaq, is regarded as the northernmost exposed part of the Nagssugtoqidian orogen and is primarily composed of leucocratic Archaean orthogneisses intercalated with supracrustal rocks, principally amphibolites and mica schist (Fig. 1b).

Amphibolites and mica schist from the Nunatarsuaq domain are strongly foliated and were interpreted to have reached middle to upper amphibolite facies conditions, which distinguishes the Nunatarsuaq domain from the adjacent Rodebay domain (Fig. 1b; Garde & Steenfelt 1999; Kokfelt 2024). The stratigraphic thickness is around 1 km and outlines an asymmetrical antiformal fold with an 8 km northern flank (Fig. 1b; Garde & Steenfelt 1999). U-Pb dating of metamorphic zircon in amphibolites within the supracrustal belt has yielded an age of 1815 ± 4 Ma (Connelly *et al.* 2006). Previous mapping distinguished between the main, relatively continuous Nunatarsuaq supracrustal belt, interpreted as predominantly or wholly Palaeoproterozoic and smaller, more discontinuous amphibolite slivers farther south that were considered Archaean (Garde & Steenfelt 1999). This interpretation formed the basis for regional correlations that placed the main Nunatarsuaq belt within the Palaeoproterozoic tectonostratigraphic framework of the northern Nagssugtoqidian orogen. However, preliminary zircon U–Pb data from lithologies within the main belt indicate that rocks previously assigned to the Palaeoproterozoic supracrustal sequence may themselves be Archaean (T.F. Kokfelt, unpublished data). If confirmed, this would invalidate the previously inferred age distinction between the main belt and the smaller southern supracrustal slivers and suggests that much – or possibly all – of the supracrustal package in the Nunatarsuaq domain may be Archaean in age. These revised protolith ages do not alter the interpretation of a shared Palaeoproterozoic metamorphic overprint at *c*. 1.82–1.81 Ga.

1.2 Field description

The Nunatarsuaq domain consists of an ENE–WSW-trending sequence of amphibolites, mica schists and grey banded orthogneiss (Fig. 2a–c). Portions are strongly tectonised, with strongly foliated gneiss, mylonitic fabrics and transposed granitic pegmatites (Fig. 2c; Kokfelt 2024). These rocks also display migmatitic

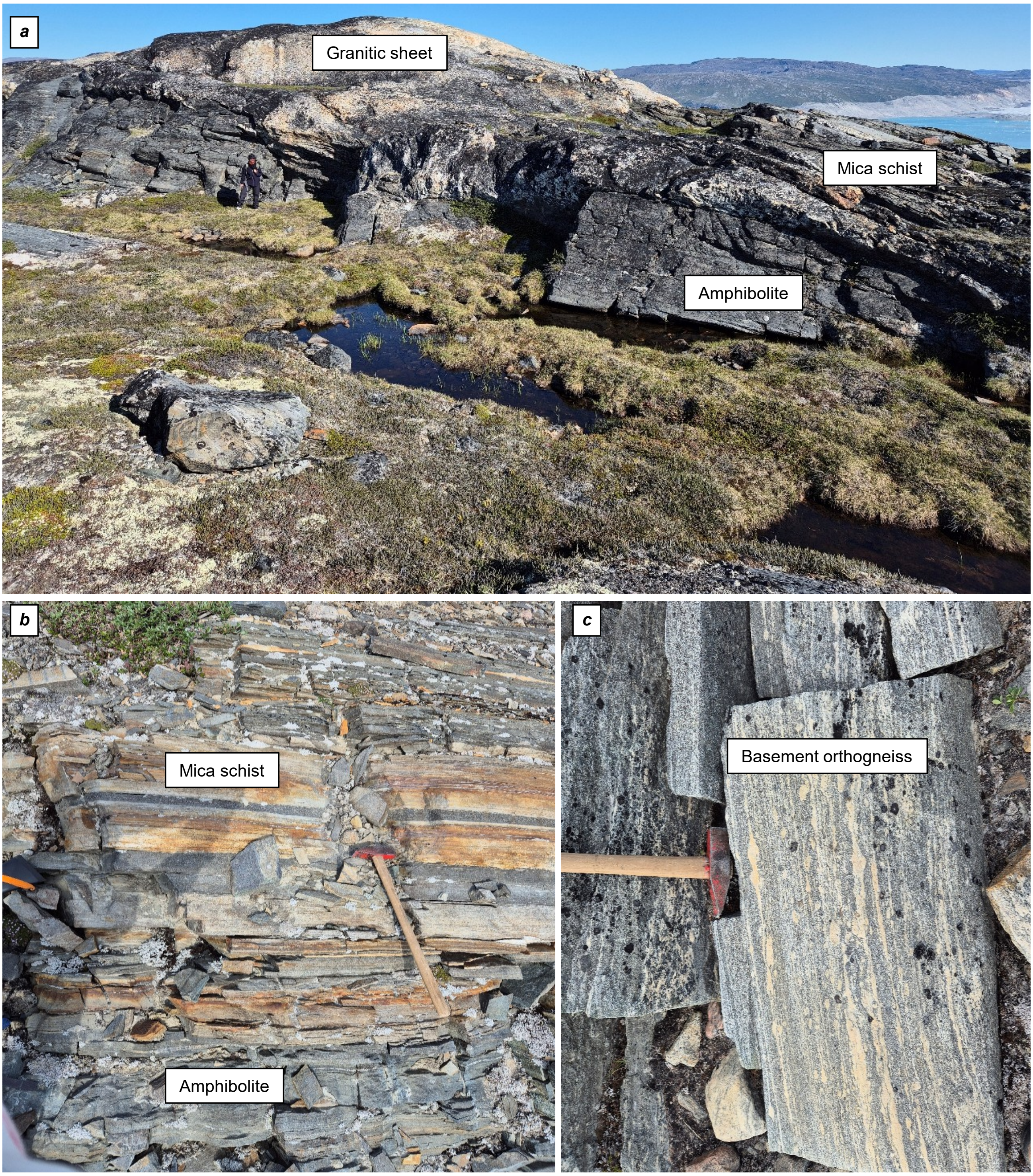

Fig. 2 Images exemplifying the rocks of the Nunatarsuaq domain. (**a**) View of the Nunatarsuaq domain showing amphibolite and mica schists intruded by concordant to weakly discordant pink granitic sheets that are locally folded and boudinaged. (**b**) Distinct alternating layers of rusty-weathering mica schists and dark amphibolite, with individual layers varying from 5 to 40 cm in thickness. (**c**) Strongly sheared basement orthogneiss.

textures, indicative of partial melting (Fig. 2c). Within the domain, pink granitic sheets occur as concordant to weakly discordant bodies that are folded or boudinaged (Fig. 2a; cf. Connelly *et al.* 2006, their fig. 7). Many of these have been classified as synkinematic (Connelly *et al.* 2006).

Amphibolites are fine- to medium-grained, dark grey and strongly foliated, with locally high biotite contents making them in places difficult to distinguish from biotite schists in the field (Fig 2a–b). Mica schists form the dominant lithology and include biotite schists, garnet–biotite schists and felsic muscovite schists (Fig. 2b).

All exhibit pervasive mm- to cm-scale compositional banding parallel to foliation.

Structural measurements across the central and eastern portion define a steeply north-dipping foliation and a gently east-plunging fold axis (Kokfelt 2024). Late brittle deformation is locally expressed by N–S-trending fractures and faults containing epidote–calcite–quartz vein fills, which cross-cut the regional foliation. A narrower slice of biotite schist and garnet-biotite schist occurs south of the main belt, whilst farther south grey banded gneisses and amphibolite units dominate.

Five samples reflecting the structural and lithological framework were selected for petrography and thermobarometry. Three of them (samples 576245, 576237 and 576232) were collected from the central–eastern area with 576237 used for *P–T* estimates (Fig. 1b). Sample 576213 was collected from within the transitional zone of schist to grey banded gneiss, and sample 576265 derives from a unit farther south, from an area interpreted to be dominated by Archaean lithologies. Together, these localities provide a representative traverse through the Nunatarsuaq domain.

2 Methods

Four mica schists and one amphibolite were chosen for analysis. The five thin sections were analysed using a Tescan Essence scanning electron microscope (SEM) at Aarhus University, Denmark. The thin sections were coated with a thin film of carbon to avoid charging when placed under the electron beam. The samples were analysed using a 20 keV, 20 nA electron beam. Using the accompanying Aztec software, Energy Dispersive Spectroscopy (EDS) spectra, element maps and element line scans were collected. Measurements were preferentially performed over a small area rather than at a single point. To ensure quantitatively reproducible data, SEM measurements were standardised using USNM 111312/444, Olivine; USNM 137041, Anorthite; USNM 133868 Anorthoclase; USNM 143965, Hornblende; USNM 143966, Microcline; R 1742, Orthopyroxene and USNM 87375, Garnet. Spectral results in oxide wt% and cations per formula unit were calculated to identify mineral phases. Element maps aided in the visualisation of mineral phases by assigning colours to certain elements enhancing their detectability.

Electron probe microanalysis (EPMA) of carbon-coated (25 nm thickness C) silicate minerals was performed with a Cameca SX100 instrument at the Department of Earth and Atmospheric Sciences, University of Alberta, Canada. The measurements were conducted using wavelength dispersive spectrometry (WDS) and Probe-for-EPMA software (Donovan *et al.* 2015) and corrected for the effects of dead-time. The operating conditions were as follows: accelerating voltage of 20 kV, beam current of 20 nA and a beam diameter of 2–10 µm on primary standards and 2–5 µm on minerals-of-interest. The following 12 elements were measured: Na, Mg, Al, Si, P, K, Ca, Ti, Cr, Mn, Fe and Ni; intensities for Mg and Al were each aggregated from two spectrometers. Count times on element peaks per spectrometer were 30 sec. Off-peak backgrounds (with total counting times equal to peak count times) were used for all elements. The X-ray lines, diffraction crystals and standards were as follows: Na *K*α, TAP, albite; Mg *K*α TAP, Frank Smith pyrope (*garnets*) or periclase (*anthophyllite*) or spinel (*remaining silicates*); Al *K*α TAP, Frank Smith pyrope (*remaining silicates*) or Gore garnet (*garnets*) or plagioclase (*amphiboles and mica*); Si *K*α TAP, Frank Smith pyrope or Gore garnet (*garnets*) or plagioclase (*amphiboles, mica, remaining silicates*); P *K*α, PET, fluorapatite; K *K*α, PET, sanidine; Ca *K*α, PET, diopside (*garnets*) or plagioclase (*remaining silicates*); Ti *K*α, PET, TiO_2; Cr *K*α, PET, Cr_2O_3; Mn *K*α, LIF, spessartine; Fe *K*α, LIF, ilmenite (*anthophyllite*) or Gore garnet (*garnets*) or fayalite (*remaining silicates*); and Ni *K*α, LIF, nickel. Interference corrections were applied to Mn for interference by Cr (Donovan *et al.* 1993). Average limits of detection determined in the Probe-for-EPMA software (Donovan *et al.* 2015) at 99% confidence ranged from 0.01 to 0.03 wt% oxide, depending on the mineral and element. Oxygen and hydroxyl contents (for amphibole and mica) were calculated by stoichiometry and included in the matrix corrections. X-ray intensity data were reduced following Armstrong (1988, 1995).

For a consistency check between methods, sample 576232 was analysed both by SEM and electron microprobe. The garnet results, for example, were as follows: $Alm_{57–66}Prp_{17–25}Grs_{11–15}Sps_{3–6}$ (SEM) and $Alm_{56–64}Prp_{17–27}Grs_{12–14}Sps_{3–6}$ by electron microprobe. The results also overlap for feldspar, amphibole and biotite.

3 Results

3.1 Petrography

Sample 576232 is a medium-grained porphyroblastic garnet amphibolite comprising foliated bands of Ca-amphibole and feldspar (Fig. 3a). Minor phases include chlorite, apatite, ilmenite, iron oxides, sulphides, anthophyllite and epidote. Garnets are porphyroblasts, reaching several millimetres in size containing abundant inclusions of feldspar, ilmenite, chlorite, apatite and quartz, which may collectively result in a patchwork texture. Anthophyllite grains are small and mostly occur together with Ca-amphibole either as adjacent mineral grains or in proximity (Fig. 4d). Ilmenite grains are frequent, can reach 1 mm in size and occur together with rarer sulphide and iron oxide phases.

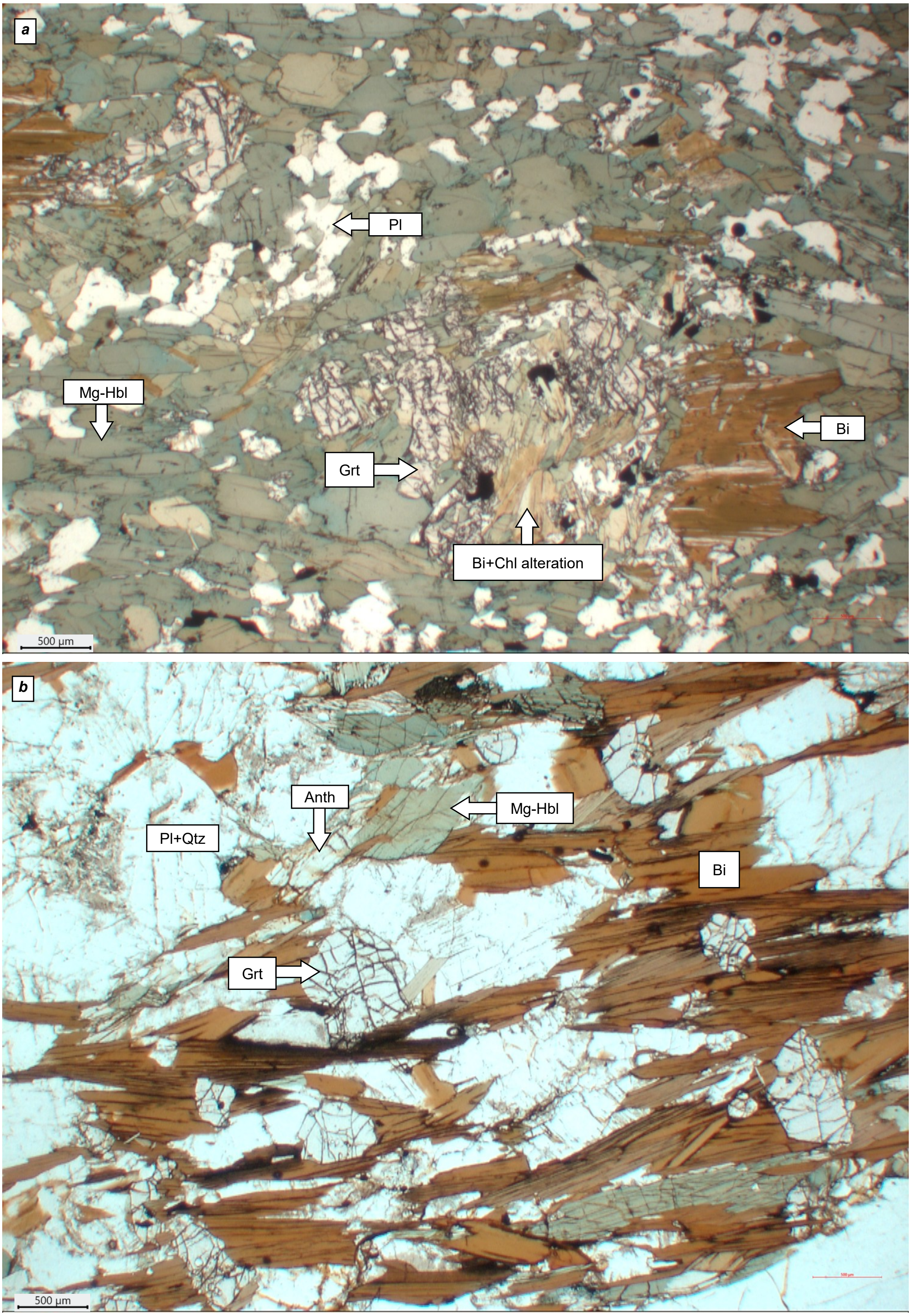

Fig. 3 Plane-polarised optical images of thin sections. (**a**) Fractured and altered garnet porphyroblast including chlorite alteration of biotite, surrounded by amphibole band in thin section of amphibolite sample 576232. (**b**) Small garnet grains in matrix composed of quartz, plagioclase, biotite and amphibole in the mica schist sample 576265. **Grt**: Garnet. **Bi**: Biotite. **Pl**: Plagioclase. **Qtz**: Quartz. **Anth**: Anthophyllite. **Mg-Hbl**: Magnesio-Hornblende.

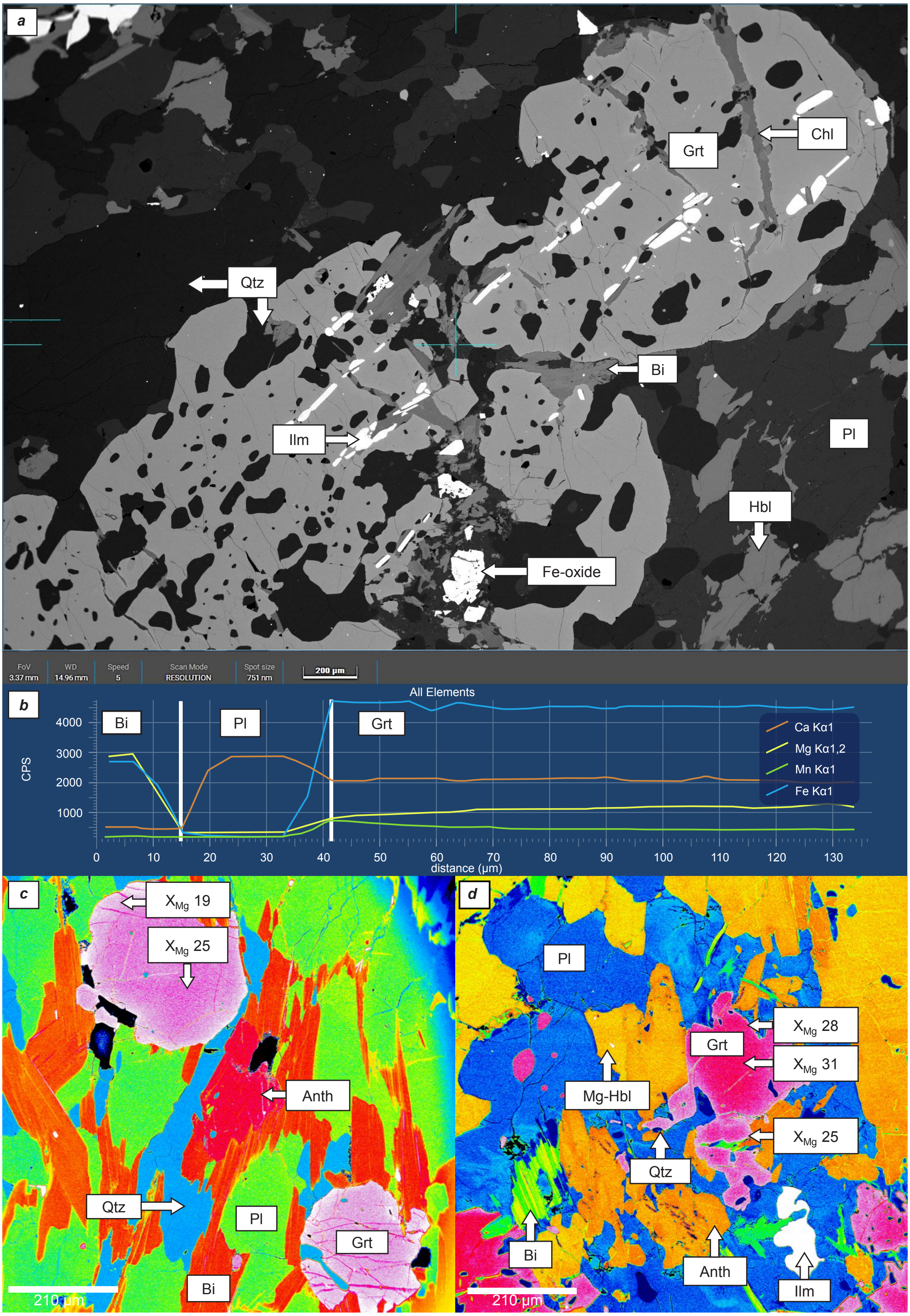

Fig. 4 (**a**) BSE image of mica schist sample 576237 showcasing a large, inclusion-rich garnet porphyroblast in a matrix composed of quartz, plagioclase and amphibole. (**b**) Line-scan across a garnet grain in mica schist sample 576213 showing little internal zoning in the core; towards the rim, Fe and Mn increase, whereas Mg and Ca decrease. The line-scan location is shown in the supplementary material. False colour enhanced back scattered image of the (**c**) mica schist sample 576265 and (**d**) the amphibolite sample 576232 showcasing garnet alteration at its rims and fractures. The false colour scale represents variations in back scattered image intensity and was generated using ImageJ software (Schneider *et al*. 2012). **Ilm**: ilmenite. **Chl**: chlorite.

Samples 576237, 576213, 576265 and 576245 are metapelitic mica schists containing combinations of garnet porphyroblasts, plagioclase, quartz, amphibole and biotite with biotite partially to be extensively replaced by chlorite (Fig. 3b). The samples are medium to strongly foliated with a distinct mineral fabric. Garnets vary in size from coarse porphyroblastic grains reaching *c*. 5 mm in sample 576237, down to small grains < 1 mm in sample 576265 (Figs 3b and 4a). Coarse grained garnets commonly contain inclusions of quartz, plagioclase, amphibole, K-feldspar, apatite, ilmenite, rutile, iron oxides, biotite, chlorite and zircon, whilst small grains typically are inclusion free. Coarse grains are commonly elongated and fractured, and fractures may be filled by chlorite veins (Fig. 4a). Biotite is widely distributed in samples 576213 and 576265, where large elongate grains reaching *c*. 4 mm in length define a distinct fabric representing *c*. 15% modal composition (Fig. 4c). In sample 576237, unaltered biotite is rare, with chlorite replacement is very frequent, and most unaltered biotite is found near garnet grains or as inclusions in garnet. In sample 576245, biotite is rare, and instead chlorite, actinolite and zoisite are present, where chlorite is tabular and defines the foliation of the rock. Feldspar is the most common mineral group in all samples, occurring as matrix and inclusions, sometimes showing alteration textures. Anthophyllite is present in samples 576213 and 576265, with grains ranging in size between *c*. 0.1 and 0.5 mm, often occurring together with Ca-amphibole oriented with the mineral fabric, and grains are occasionally fractured with inclusions of quartz and feldspar (Fig. 4d).

3.2 Mineral chemistry

3.2.1 Garnet

Within the mica schists, garnet grains show limited chemical variation, with core compositions falling within the almandine group ($Alm_{63–72}Prp_{11–24}Grs_{8–14}Sps_{2–8}$, $X_{Mg\ 20–24}$; Table 1, Fig. 5b). Throughout the internal part of the crystal, garnets display limited to no major component zonation (Table 1, Figs 4b–c and 5b). Near rims and fractures, garnet compositions commonly display a reverse zoning with slight increases in Fe and Mn that correspond to a decrease in the Mg content ($Alm_{67–74}Prp_{12–17}Grs_{9–14}Sps_{9–14}$, $X_{Mg15–20}$). In the garnet amphibolite (576232), garnet grains are internally unzoned and slightly more Mg-rich compared to grains analysed in the mica schist whilst still falling within the almandine compositional range ($Alm_{57}Prp_{26}Grs_{14}Sps_{3}$; Table 1, Fig. 5b). Like the mica schists, garnets in the amphibolite are commonly enriched in Mn and Fe and depleted in Mg along rims and fractures (Fig. 4d).

3.2.2 Feldspar

Feldspars are primarily andesine ($Ab_{60–66}An_{34–38}$) throughout the mica schist samples 576237, 576213 and 576265 (Fig. 5a). Sample 576245 shows a broader compositional range within the labradorite-andesine field ($Ab_{41–57}An_{43–59}$), with the labradorite variety mostly occurring as inclusions in garnet and quartz. K-feldspar is rarely found as small alterations in plagioclase grains or as inclusions in garnet grains.

In the garnet amphibolite sample (576232), feldspars show a range of compositions, mostly within the andesine-labradorite compositional range (Table 1, Fig. 5a). Sodic feldspars ($Ab_{95}An_{5}$) occur rarely as layers/mantles around some feldspar grains, often in contact with chlorite and amphibole. In some grains, a more calcic labradorite feldspar ($Ab_{32}An_{68}$) occurs in proximity to fractures.

3.2.3 Ca-amphibole

Ca-amphiboles fall within the magnesio-hornblende or ferro-hornblende compositional range. In mica schists, magnesio-hornblende has X_{Mg} values of 47–51, and ferro-hornblende has X_{Mg} values of 42–44, whereas magnesio-hornblende in the garnet amphibolite has X_{Mg} values of 55–61. Amphiboles in mica schist sample 576245 are actinolite (Table 1, Fig. 5c).

In both the mica schists and garnet amphibolite, the Mg-Fe-Mn amphibole falls within the anthophyllite compositional range. Overall, anthophyllite shows limited chemical variation, with X_{Mg} values of 50–55 (Table 1, Fig. 5d). Anthophyllite in the garnet amphibolite is similar in composition to the mica schist with X_{Mg} values slightly higher at 58–59.

3.2.4 Biotite

Biotite in the mica schist samples 576213, 576265 and 576237 is characterised by relatively low X_{Mg} values of 49–54 and TiO_2 contents of 1.0–2.5 wt%, whereas the only unaltered biotite found in mica schist sample 576245 has a higher X_{Mg} value of 63 and a TiO_2 value of 1.8 wt%. Biotite from the amphibolite sample 576232 shows higher X_{Mg} values of 59–64 and lower TiO_2 values of 0.7–1.4 wt% (Table 1).

3.3 Geothermobarometry

Temperatures and pressures were estimated from mineral compositions in samples 576265, 576213 and 576237 using the garnet–biotite thermometer and the garnet–biotite–plagioclase–quartz (GBPQ) geobarometer (Wu *et al.* 2004). The random error of the GBPQ geothermobarometer (±1.2 kbar) is estimated from numerical modelling of a data-set assuming an input temperature error of ±50°C and analytical error of

Table 1 Representitative mineral analysis of anthophyllite- and garnet-bearing amphibolite and metapelites.

Mineral:	Garnet										Biotite					Ferro-hbl5
Sample:	576237(SEM)		576213(EPMA)		576265(EPMA)		576232(EPMA)		576245(SEM)		576237	576213	576265	576232	576245	576237
Location:	Core	Rim	Core	Rim	Core	Rim	Core	Rim	Core	Rim	Matrix	Matrix	Matrix	Matrix	Matrix	Matrix
SiO_2	37.56	37.78	37.96	37.61	37.85	37.41	38.54	38.06	36.73	37.64	35.90	37.91	36.84	36.62	36.86	43.63
TiO2						0.11					1.74	2.26	1.60	0.88	1.82	0.6
Al_2O_3	21.21	21.4	21.79	21.44	21.60	21.32	21.81	21.40	22.02	22.51	16.87	17.23	16.94	18.20	16.95	15.02
FeO	32.48	32.23	29.02	29.95	29.55	30.33	26.18	28.65	30.65	29.29	20.37	18.88	18.74	16.23	15.46	19.35
Fe_2O_3 / calc									1.16	1.94						
MnO	0.86	0.82	1.22	2.12	1.21	3.43	1.57	2.72	0.74	1.7			0.11	0.08		
MgO	4.42	3.83	4.90	3.47	5.25	3.06	6.57	4.30	4.63	4.34	10.92	12.62	12.09	14.51	14.47	7.83
CaO	2.98	4.2	4.93	4.94	4.14	4.11	4.94	4.62	3.33	4.27	0.11	0.04	0.04	0.03		10.42
Na_2O									0.2	0.17	0.11	0.17	0.10	0.06	0.17	1.65
K_2O											8.68	8.46	9.41	9.22	8.61	0.34
H_2O^4											3.91	4.01	3.98	4.04	4.00	2.03
Total	99.51	100.26	99.81	99.53	99.60	99.77	99.61	99.75	99.46	101.86	98.61	101.58	99.83	99.88	98.34	100.87
Oxygens	12	12	12	12	12	12	12	12	12	12	11	11	11	11	11	23
Si^{4+}	3.00	3.00	2.99	3.00	2.99	3.00	3.01	3.02	2.92	2.93	2.76	2.78	2.78	2.72	2.77	6.45
Al^{3+}	2.00	2.00	2.02	2.02	2.01	2.01	2.00	2.00	2.06	2.07	1.53	1.49	1.50	1.59	1.50	2.62
Ti^{4+}						0.01					0.10	0.12	0.09	0.05	0.10	0.07
Fe^{2+}	2.17	2.14	1.91	2.00	1.95	2.03	1.71	1.90	2.04	1.90	1.31	1.16	1.18	1.01	0.97	2.39
Fe^{3+}									0.07	0.11						
Mn^{2+}	0.06	0.06	0.08	0.14	0.08	0.23	0.10	0.18	0.05	0.11			0.01	0.01		
Mg^{2+}	0.53	0.45	0.58	0.41	0.62	0.37	0.76	0.51	0.55	0.51	1.25	1.38	1.36	1.61	1.62	1.73
Ca^{2+}	0.25	0.36	0.42	0.42	0.35	0.35	0.41	0.39	0.28	0.36	0.01	0.02				1.65
Na^{+}									0.03	0.03	0.02	0.79	0.01	0.01	0.02	0.47
K^{+}											0.85		0.90	0.87	0.82	0.06
Total	8.00	8.00	8.00	7.99	7.99	8.00	8.00	8.00	8.01	8.01	7.81	7.75	7.84	7.87	7.81	15.44
Alm[1]	72	74	64	67	65	68	57	64	70	66						
Prp	17	15	19	14	21	12	26	17	19	18						
Grs	8	9	14	14	12	12	14	13	10	12						
Sps	2	2	3	5	3	8	3	6	2	4						
An[3]																
Ab																
Or																
X_{Mg}[2]	20	17	23	17	24	15	31	21	21	21	49	54	53	61	63	42

Table 1 Continued.

Mineral:	Magnesio-hornblende			Anthophyllite			Actinolite	Feldspar								
Sample:	576213	576265	576232	576213	576265	576232	576245	576237			576213	576265	576232		576245	
Location:	Matrix	Matrix	Matrix	Matrix	Matrix	Matrix	Matrix	Matrix	K-rich inclusion	Na-rich inclusion	Matrix	Matrix	Ca-rich variation	Matrix	Matrix	K-rich inclusion
SiO_2	45.10	44.74	45.33	53.77	54.06	55.30	52.75	58.73	64.51	61.87	59.27	59.67	50.54	54.82	52.82	65.15
TiO_2	0.66	0.65	0.46				0.12									
Al_2O_3	11.95	12.90	13.17	1.36	0.97	0.88	3.41	25.67	18.47	24.54	25.96	25.76	31.87	28.91	30.38	18.98
FeO	16.84	17.28	13.73	24.73	25.65	22.49	11.60	0.10	0.84	0.48	0.03	0.08	0.11	0.12	0.24	0.33
Fe_2O_3 / calc	0.85						1.98									
MnO	0.39	0.30	0.20	0.49	0.84	0.70	0.19									
MgO	10.50	9.87	11.98	16.63	16.28	18.51	15.65		0.21							
CaO	10.56	10.95	11.13	0.73	0.74	0.70	12.41	7.46		5.27	7.29	7.12	13.98	10.66	11.45	
Na_2O	1.10	1.17	1.41	0.05	0.08	0.04	0.33	7.84		8.25	7.42	7.51	3.63	5.46	4.95	0.14
K_2O	0.34	0.32	0.21						15.80	0.08	0.06	0.04	0.01	0.03		15.72
H_2O[4]	2.03	2.03	2.06	2.05	2.03	2.07	2.10									
Total	100.33	100.21	99.68	99.81	100.64	100.7	100.54	99.80	99.83	100.49	100.03	100.18	100.14	100.00	99.84	100.32
Oxygens	23	23	23	23	23	23	23	8	8	8	8	8	8	8	8	8
Si^{4+}	6.65	6.60	6.62	7.89	7.91	7.95	7.55	2.63	2.99	2.73	2.64	2.65	2.30	2.47	2.39	2.99
Al^{3+}	2.08	2.24	2.27	0.24	0.17	0.15	0.58	1.36	1.01	1.28	1.36	1.35	1.71	1.54	1.62	1.03
Ti^{4+}	0.07	0.07	0.05				0.01									
Fe^{2+}	2.08	2.13	1.68	3.03	3.14	2.70	1.39		0.03	0.02					0.01	0.01
Fe^{3+}	0.10						0.21									
Mn^{2+}	0.05	0.04	0.02	0.06	0.10	0.09	0.02									
Mg^{2+}	2.31	2.17	2.61	3.63	3.55	3.97	3.34		0.01							
Ca^{2+}	1.67	1.73	1.74	0.11	0.12	0.11	1.90	0.36		0.25	0.35	0.34	0.68	0.51	0.56	
Na^{+}	0.32	0.33	0.40	0.01	0.01	0.01	0.09	0.68		0.71	0.64	0.65	0.32	0.48	0.43	0.01
K^{+}	0.06	0.06	0.04						0.93	0.005						0.92
Total	15.38	15.37	15.42	14.98	14.99	14.97	15.09	5.03	4.98	4.99	4.99	4.99	5.00	5.00	5.01	4.96
Alm[1]																
Prp																
Grs																
Sps																
An[3]								34	0	26	35	34	68	52	56	0
Ab								66	0	74	65	66	32	48	44	1
Or								0	100	0	0	0	0	0		99
X_{Mg}[2]	47	50	61	55	53	59	71									

[1]Garnet endmembers: Alm = Almandine = 100*Fe/(Fe + Mg + Ca + Mn); Prp = Pyrope = 100*Mg/(Ca + Mg + Fe + Mn); Grs = Grossular = 100*Ca/(Ca + Mg + Ca + Mn); Sps = Spessartine = 100*Mn/(Fe + Mg + Fe + Mn).
[2]X_{Mg} = 100*Mg/(Mg + Fe^{2+}). [3]Feldspar endmembers: An = Anorthite = 100*Ca/(Ca + Na + K); Ab = Albite = 100*Na/(Ca + Na + K); Or = Orthoclase = 100*K/(Ca + Na + K). [4]H_2O was calculated based on stoichiometry.
[5]Ferro-Hbl: Ferro-Hornblende. Samples 576237 and 576245 analysed by SEM. Samples 576213, 576232 and 576265 analysed by EPMA.

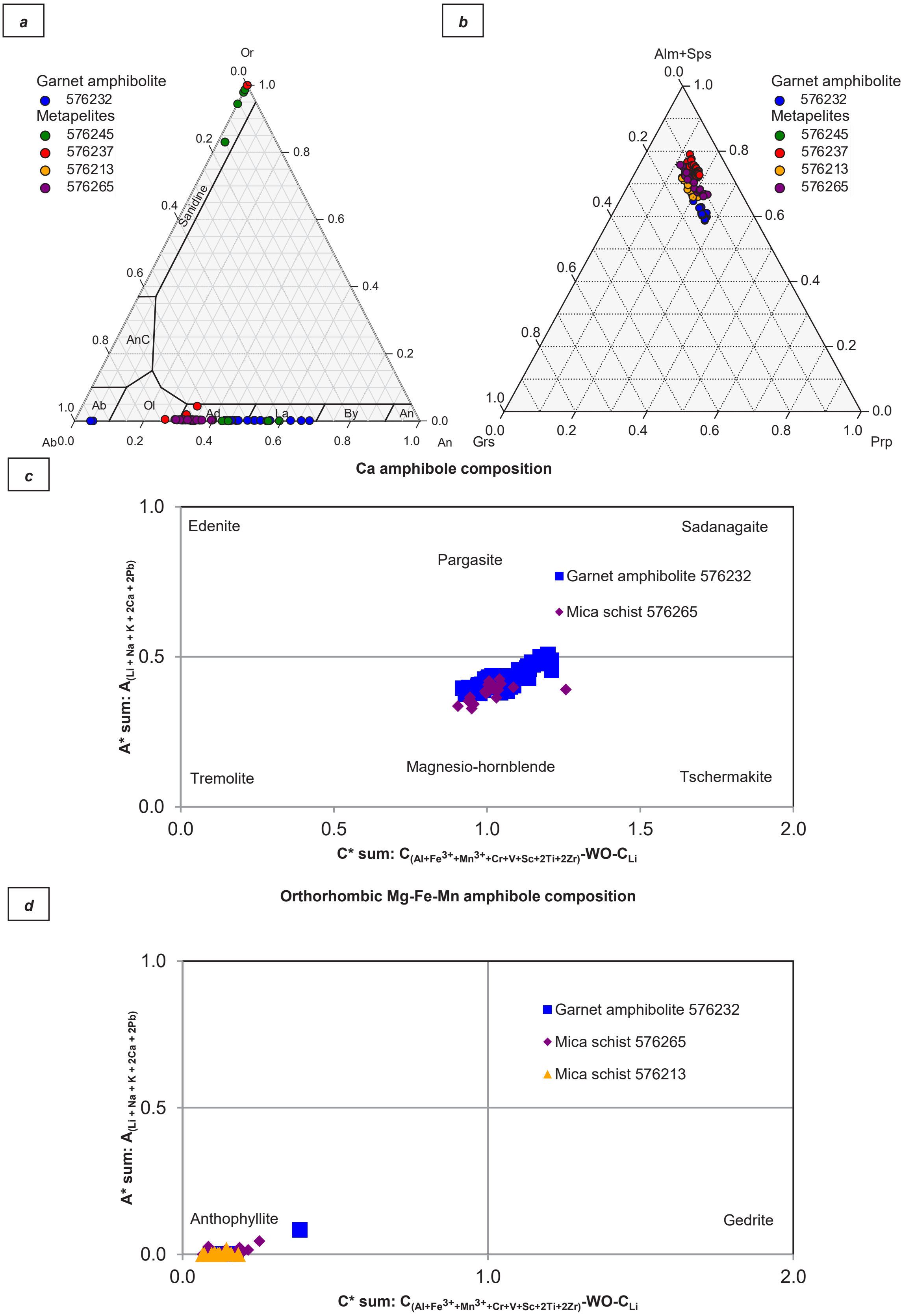

Fig. 5 Mineral compositional data for amphibolite sample 576232 and metapelitic mica schist samples 576213, 576237, 576245 and 576265. Feldspar and garnet diagrams were produced using Thermobar (Wieser *et al*. 2022), and the amphibole classification follows Hawthorne *et al*. (2012) with diagrams produced after Graham & Midgley (2000). (**a**) Feldspar compositions showing dominantly andesine compositions with minor retrograde albite rims in the sample 576232. (**b**) Garnet compositions showing predominantly almandine-rich garnets with limited core zoning and Mn-enriched retrograde rims. (**c**) Ca-amphibole compositions showing dominantly magnesio-hornblende to ferro-hornblende, with actinolite restricted to the sample 576245. (**d**) Orthorhombic amphibole compositions plot in the anthophyllite field.

±5% in Ca and Al contents of garnet, biotite and plagioclase (Wu *et al.* 2004). Due to the frequent occurrence of ilmenite and the rare presence of haematite in the sample, the Fe^{3+} content was estimated at 0.116% (Wu *et al.* 2004). The lack of compositional zoning in the centre of garnets indicates diffusional homogenisation at high temperature metamorphism. In contrast, the frequent occurrence of Mg depletion and Mn enrichment along garnet rims and fractures likely indicates a retrograde alteration of peak temperature garnet compositions (Mazur *et al.* 2012; Gulbin 2013). Garnet core compositions are therefore interpreted to represent equilibrium compositions and chosen for GBPQ analysis, together with unaltered biotite and plagioclase grains in proximity to the corresponding equilibrium garnet pairs. From sample 576265, a total of eight mineral pairs yields an average temperature of 751°C with a standard deviation of 17°C (2.2%) and an average pressure of 9.4 kbar with a standard deviation of 0.6 kbar (6.4%; Fig. 6), which is less than the error inherent to the geothermobarometer (±1.2 kbar, Wu *et al.* 2004). From sample 576213, six sets of mineral pairs yield an average temperature of 702°C with a standard deviation of 17°C (2.4%) and an average pressure of 9.4 kbar with a standard deviation of 0.3 kbar (3.6%; Fig. 6). From the sample 576237, seven sets of mineral pairs yield an average temperature of 710°C with a standard deviation of 26°C (3.7%) and an average pressure of 7.9 kbar with a standard deviation of 0.27 kbar (3.4%; Fig. 6). The GBPQ thermobarometer was not applied to the garnet amphibolite (576232) due to the lack of quartz as a matrix constituting phase.

4 Discussion

4.1 Metamorphic evolution

Thermobarometric data from three structurally distinct samples define a narrow range of upper amphibolite facies conditions at *c.* 700–750°C and *c.* 8–9.5 kbar, corresponding to burial at mid- to lower-crustal depths. The coexistence of anthophyllite and hornblende is

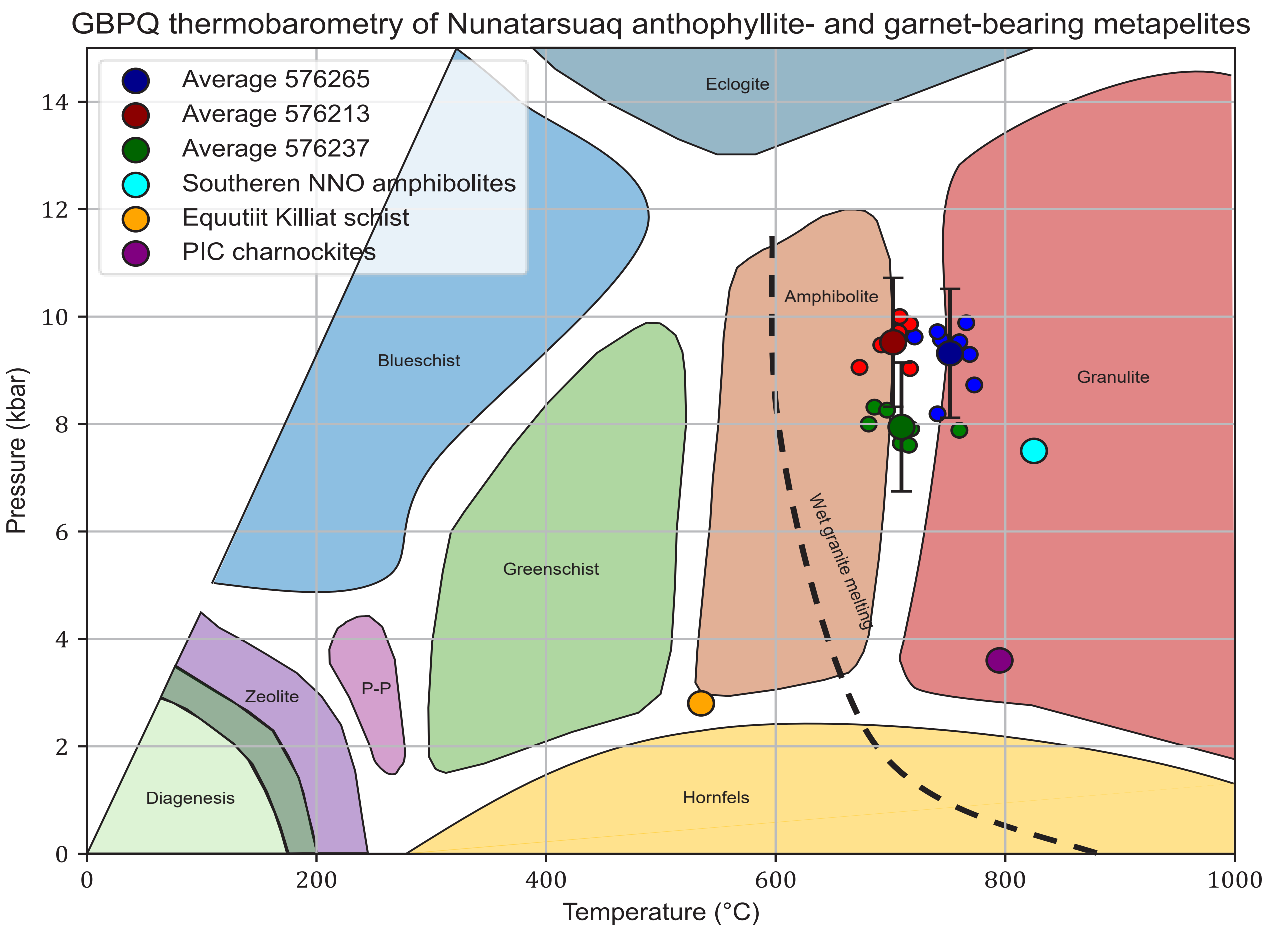

Fig. 6 Results of GBPQ thermobarometric calculations for Nunatarsuaq metapelites along with published thermobarometric calculations for direct comparison (Garde & Hollis 2010; Mazur *et al*. 2012; Dziggel *et al*. 2025). **NNO**: northern Nagssugtoqidian orogen. **PIC**: Prøven igneous complex. Metamorphic facies and wet granite melting line (Boettcher & Wyllie 1968; Bucher 2023). **Black error bars** indicate inherent error in the barometer (±1.2 kbar; Wu *et al*. 2004).

compatible with high-temperature stability of orthorhombic amphibole and does not require low-grade peak conditions, as is commonly assumed for anthophyllite-bearing assemblages (Schumacher 2007). The garnet-biotite-plagioclase-quartz-bearing assemblages across the Nunatarsuaq domain yield essentially indistinguishable *P–T* conditions, indicating that the samples, despite their differing structural positions, equilibrated at similar mid–lower-crustal depths during peak metamorphism. However, the slightly lower pressures recorded by sample 576237 relative to the more southern samples 576265 and 576213 may reflect modest decompression at broadly constant temperature during or shortly after peak metamorphism.

In geological time, the *P–T* evolution is linked to the Nagssugtoqidian orogeny. The timing of peak metamorphism is constrained by synkinematic granites at 1821 ± 4 Ma, an 1815 ± 4 Ma metamorphic zircon in an amphibolite (Connelly *et al.* 2006), and more recently identified zircon overgrowths in regional gneisses yielding ages of 1816 ± 15 Ma and 1817 ± 19 Ma (T. F. Kokfelt, unpublished data 2026). Collectively, these data indicate that peak metamorphism occurred at *c*. 1.82–1.81 Ga and affected rocks across the Nunatarsuaq domain irrespective of protolith age.

Hornblende ^{39}Ar–^{40}Ar dating in the Qeqertarsuup Tunua and eastern Nuussuaq region has yielded ages ranging from *c.* 1750 to 1925 Ma (Rasmussen & Holm 1999), whilst an age from the Nunatarsuaq domain of 1740 Ma (Willigers *et al.* 2002) indicates the domain cooled below the amphibole closure temperature of *c*. 580°C at this time. Combined with peak temperatures of *c*. 750°C at *c*. 1820 Ma, these data imply a relatively slow cooling rate of *c*. 2–3°C/Myr. Together with the *P–T* clustering and the largely unzoned character of garnet, this is consistent with prolonged residence at mid- to lower-crustal levels, following peak metamorphism rather than a short-lived thermal pulse (Caddick *et al.* 2010). Moreover, the high temperatures are above the granite wet-melting point and would facilitate partial melting, which is consistent with the presence of synkinematic granitic dikes and widespread migmatitic textures observed in banded gneisses (Fig. 2).

Textural evidence points to a subsequent retrograde evolution in the studied samples. Mn-enriched garnet rims and fracture-controlled Mn enrichment, together with the partial replacement of biotite by chlorite and the growth of epidote and actinolite in mica schists, document hydration and cooling from upper amphibolite towards greenschist facies conditions (Gulbin 2013). Finally, epidote-calcite-quartz vein fills in late N–S-trending brittle fractures and faults demonstrate a younger, low-temperature fluid overprint.

4.2 Regional implications

The recognition of upper amphibolite facies conditions in the Nunatarsuaq domain represents the first quantitative *P–T* constraints by *c*. 700–750°C at *c*. 8–9.5 kbar from the northernmost part of the Nagssugtoqidian orogen, which was described only qualitatively as 'amphibolite facies' by Garde & Steenfelt (1999). In the broader regional context, the Nunatarsuaq conditions lie between those of the granulite facies core of the orogen (Davidson 1979; Connelly *et al.* 2000; Korstgård *et al.* 2006) and the lower-grade amphibolite to greenschist facies rocks to the south-west and north. For example, amphibolites immediately north of the granulite–amphibolite transition zone record peak temperatures of 810–840°C at *c*. 7.5 kbar (Mazur *et al.* 2012), whereas staurolite schists from the Isuamiut–Qaqqarsuatsiaq–Equutiit Killiat islands yield markedly lower *P–T* estimates of 520–550°C at 2.6–3.0 kbar (Garde & Hollis 2010; Figs 1 and 6). Similarly, the supracrustal belt on the Kangilinaaq peninsula, *c*. 60 km to the south-west, has been classified as lower amphibolite facies (Hollis *et al.* 2006), although no quantitative *P–T* data exist for direct comparison.

North of Nunatarsuaq, the Disko Bugt–Nuussuaq segment of the Rinkian fold belt exhibits a northward increasing metamorphic gradient ranging from greenschist to upper amphibolite facies (Connelly *et al.* 2000). Farther north again, granulite facies charnockites of the Prøven igneous complex record *P–T* estimates of 785–805°C at 3.4–4.0 kbar (Figs 1 and 6) (Dziggel *et al.* 2025). Within this regional framework, the Nunatarsuaq *P–T* results reveal an unexpectedly high-grade domain situated at the northern margin of the Nagssugtoqidian orogen, rather than representing a low-grade fringe. The presence of upper amphibolite facies assemblages in rocks from across the domain, combined with their similar mineral chemistry and deformation fabrics, suggests that these units experienced a shared metamorphic event, most plausibly associated with Palaeoproterozoic crustal thickening and burial during collision of the Rae and North Atlantic cratons.

Taken together, these findings refine the metamorphic architecture of the northern Nagssugtoqidian orogen. Rather than a monotonic decrease in metamorphic grade away from the granulite facies core, the Nunatarsuaq results indicate localised preservation of mid- to lower-crustal metamorphic conditions farther to the north and highlight the structural and thermal complexity of the orogen. Additional geochronological and structural works in the wider Ilulissat region will be needed to delineate the extent of this high-grade domain and to clarify its relationship to the Aasiaat domain, the central Nagssugtoqidian and the northern region of Qeqertarsuup Tunua.

5 Conclusions

The petrographic and thermobarometric data presented here provide the first quantitative constraints on the conditions of metamorphism in the Nunatarsuaq domain in the northernmost part of the Nagssugtoqidian orogen. SEM and EPMA analyses of mineral assemblages including coexisting hornblende and anthophyllite, together with largely unzoned garnet, demonstrate high-temperature re-equilibration and support Palaeoproterozoic peak metamorphic conditions at *c*. 700–750°C and *c*. 8–9.5 kbar. The shared metamorphic grade, mineral assemblages and deformation fabrics across the Nunatarsuaq domain indicate burial to mid–lower-crustal depths including partial melting and metamorphism at upper amphibolite facies, most plausibly associated with crustal thickening during collision between the Rae and North Atlantic cratons at *c*. 1.82–1.81 Ga. Retrograde chlorite, epidote and actinolite record subsequent cooling and hydration during exhumation into lower amphibolite to greenschist facies conditions.

These findings reveal that the Nunatarsuaq domain preserves a higher-grade metamorphic imprint than previously recognised and refine the metamorphic architecture of the northern Nagssugtoqidian orogen.

Acknowledgments

This study is a contribution to the Ilulissat Mapping Project, led by the Geological Survey of Denmark and Greenland (GEUS) and co-funded by the Ministry of Mineral Resources (MMR), Government of Greenland. Fieldwork in 2024 was conducted by TFK and KT with support from Høgni Vesturklett and Fie Krøyer (GEUS). We thank Høgni Vesturklett for handling and cutting the samples used for thin section preparation. We also thank reviewers Adam Garde, Sampriti Basak and Tomas Naeraa for constructive and helpful comments, which have improved the final work.

Additional information

Funding statement

This study was supported by the Geological Survey of Denmark and Greenland (GEUS) and Ministry of Mineral Resources, Government of Greenland, as well as the Institut for Geoscience, Aarhus University, Denmark.

Author contributions

Conceptualisation: VOE, JMS, TFK. Formal analysis: VOE, AJL, JMS, TRJ, TEW; Funding: JMS, TFK. Investigation: VOE, JMS, AJL, KT, TFK, TEW. Visualisation: VOE, TEW, JMS, AJL; Writing: VOE, JMS, TEW, AJL, TFK, KT.

Competing interests

The authors declare no competing interests.

Additional files

Two additional files are available as supplementary information at *https://doi.org/10.22008/FK2/VIJJS0*. SEM and EPMA data are available, sorted by sample, in an accompanying Excel file Supplementary File S1.xlsx. Precision of standards are available in Supplementary File S2.xlsxl.

References

Armstrong, J.T. 1988: Quantitative analysis of silicate and oxide materials: Comparison of Monte Carlo, ZAF and φ(ρz) procedures. Microbeam Analysis **1**, 239–246.

Armstrong, J.T. 1995: CITZAF: A package of correction programs for the quantitative electron microbeam X-ray-analysis of thick polished materials, thin-films, and particles. Microbeam Analysis **4**, 177–200.

Boettcher, A.L. & Wyllie, P.J. 1968: Melting of granite with excess water to 30 kilobars pressure. The Journal of Geology **76**(2), 235–244. *https://doi.org/10.1086/627324*

Bucher, K. 2023: Petrogenesis of metamorphic rocks. Springer International Publishing. *https://doi.org/10.1007/978-3-031-12595-9*

Caddick, M.J., Konopásek, J. & Thompson, A.B. 2010: Preservation of garnet growth zoning and the duration of prograde metamorphism. Journal of Petrology **51**(11), 2327–2347. *https://doi.org/10.1093/petrology/egq059*

Connelly, J.N. & Thrane, K. 2005: Rapid determination of Pb isotopes to define Precambrian allochthonous domains: An example from West Greenland. Geology **33**, 953–956. *https://doi.org/10.1130/G21720.1*

Connelly, J.N., Thrane, K., Krawiec, A.W. & Garde, A.A. 2006: Linking the Palaeoproterozoic Nagssugtoqidian and Rinkian orogens through the Disko Bugt region of West Greenland. Journal of the Geological Society **163**, 319–335. *https://doi.org/10.1144/0016-764904-115*

Connelly, J.N., Van Gool, J.A.M. & Mengel, C.M. 2000: Temporal evolution of a deeply eroded orogen: The Nagssugtoqidian Orogen, West Greenland. Canadian Journal of Earth Sciences **37**(8): 1121–1142. *https://doi.org/10.1139/e00-032*

Davidson, L.M. 1979: Nagssugtoqidian granulite facies metamorphism in the Holsteinsborg region, West Greenland. Rapport Grønlands Geologiske Undersøgelse **89**, 97–108. *https://doi.org/10.34194/rapggu.v89.7570*

Donovan, J.J., Kremser, D., Fournelle, J.H. & Goemann, K. 2015: Probe for EPMA: Acquisition, automation and analysis. Eugene, OR: Probe Software Inc. *www.probesoftware.com*

Donovan, J.J., Snyder, D.A. & Rivers, M.L. 1993: An improved interference correction for trace element analysis. Microbeam Analysis **2**, 23–28. *https://doi.org/10.1017/S0424820100132868*

Dziggel, A., Bramm, L., Kokfelt, T.F., Grocott, J. & Diener, J.F.A. 2025: Preservation of igneous and metamorphic charnockites in the Palaeoproterozic Prøven Igneous Complex, Rinkian Orogen, central West Greenland. Precambrian Research **417**, 107634. *https://doi.org/10.1016/j.precamres.2024.107634*

Garde, A.A. & Hollis, J.A. 2010: A buried Palaeoproterozoic spreading ridge in the northern Nagssugtoqidian orogen, West Greenland. Geological Society **338**(1), 213–234. *https://doi.org/10.1144/SP338.11*

Garde, A.A. & Steenfelt, A. 1999: Precambrian geology of Nuussuaq and the area north-east of Disko Bugt, West Greenland. Geology of Greenland Survey Bulletin **181**, 6–40. *https://doi.org/10.34194/ggub.v181.5108*

Glassley, W.E., Korstgård, J.A., Sørensen, K. & Platou, S.W. 2014: A new UHP metamorphic complex in the ~1.8 Ga Nagssugtoqidian Orogen of West Greenland. American Mineralogist **99**(7), 1315–1334. *https://doi.org/10.2138/am.2014.4726*

Graham, D.J. & Midgley, N.G. 2000: Graphical representation of particle shape using triangular diagrams: An Excel spreadsheet method. Earth Surface Processes and Landforms **25**(13), 1473–1477. *https://doi.org/10.1002/1096-9837(200012)25:13%3C1473::AID-ESP158%3E3.0.CO;2-C*

Guarnieri, P., Rosa, D., Thrane, K., Kokfelt, T.F., Sørensen, E.V., DeWolfe, M.Y. & Baker, N. 2023: Tectonics of the Palaeoproterozic Rinkian orogen, central West Greenland. GSA Bulletin **136**(5–6), 2596–2615. *https://doi.org/10.1130/B36930.1*

Gulbin, Y.L. 2013: Modeling of zoning patterns in garnet: Thermodynamic and kinetic aspects. Geology of Ore Deposits **55**(8), 625–636. *https://doi.org/10.1134/S1075701513080035*

Hawthorne, F.C., Oberti, R., Harlow, G.E., Maresch, W.V., Martin, R.F., Schumacher, J.C. & Welch, M.D. 2012: Nomenclature of the amphibole supergroup. American Mineralogist **97**, 2031–2048. *https://doi.org/10.2138/am.2012.4276*

Hollis, J.A., Keiding, M., Stensgaard, B.M., van Gool, J.A.M. & Garde, A.A. 2006: Evolution of Neoarchaean supracrustal belts at the northern margin of the North Atlantic Craton, West Greenland. GEUS Bulletin **11**, 9–32. *https://doi.org/10.34194/geusb.v11.4914*

Kokfelt, T.F. 2024: Report of the fieldwork carried out during the summer of 2024 within the framework of the Ilulissat mapping project, 72 pp. Unpublished field report, Geological Survey of Denmark and Greenland (GEUS).

Kokfelt, T.F. *et al*. 2023: Seamless digital 1:500 000 scale geological map of Greenland, version 3.0. GEUS Dataverse. *https://doi.org/10.22008/FK2/FWX5ET*

Korstgård, J.A., Stensgaard, B.M. & Rasmussen, T.M. 2006: Magnetic anomalies and metamorphic boundaries in the southern Nagssugtoqidian orogen, West Greenland. GEUS Bulletin **11**, 179–184. *https://doi.org/10.34194/geusb.v11.4930*

Mazur, S., Anczkiewicz, R., Szczepański, J., van Gool, J.A.M. & Thirlwall, M. 2012: Palaeoproterozoic metamorphism and cooling of the northern Nagssugtoqidian orogen, West Greenland. Precambrian Research **196–197**, 171–192. *https://doi.org/10.1016/j.precamres.2011.12.005*

Mazur, S., Piazolo, S. & Alsop, G.I. 2006: Structural analysis of the northern Nagssugtoqidian orogen, West Greenland: An example of complex tectonic patterns in reworked high-grade metamorphic terrains. GEUS Bulletin **11**, 163–178. *https://doi.org/10.34194/geusb.v11.4929*

Rasmussen, H. & Holm, P.M. 1999: Proterozoic thermal activity in the Archaean basement of the Disko Bugt region and eastern Nuussuaq, West Greenland: Evidence from K-Ar and 40Ar-39Ar mineral age investigations. Geology of Greenland Survey Bulletin **181**, 55–64. *https://doi.org/10.34194/ggub.v181.5113*

Sanborn-Barrie, M., Thrane, K., Wodicka, N. & Rayner, N. 2017: The Laurentia-West Greenland connection at 1.9 Ga: New insights from the Rinkian fold belt. Gondwana Research **51**, 289–309. *https://doi.org/10.1016/j.gr.2017.07.002*

Schneider, C., Rasband, W. & Eliceiri, K. 2012: NIH Image to ImageJ: 25 years of image analysis. Nature Methods **9**, 671–675. *https://doi.org/10.1038/nmeth.2089*

Schönig, J., Benner, C., Meinhold, G., von Eynatten, H. & Lünsdorf, K. 2023: Detrital garnet petrology challenges Palaeoproterozic UHP metamorphism in Western Greenland, EGU General Assembly 2023, Vienna, Austria, 23–28 Apr 2023, EGU23-12621. *https://doi.org/10.5194/egusphere-egu23-12621*

Schumacher, J.C. 2007: Metamorphic amphiboles: Composition and coexistence. Reviews in Mineralogy and Geochemistry **67**(1), 359–416. *https://doi.org/10.2138/rmg.2007.67.10*

Thrane, K. 2021: The oldest part of the Rae craton identified in western Greenland. Precambrian Research **357**, 106139. *https://doi.org/10.1016/j.precamres.2021.106139*

van Gool, J.A.M., Connelly, J.N., Marker, M. & Mengel, F.C. 2002: The Nagssugtoqidian Orogen of West Greenland: Tectonic evolution and regional correlations from a West Greenland perspective. Canadian Journal of Earth Sciences **39**(5), 665–686. *https://doi.org/10.1139/e02-027*

Wieser, P., Petrelli, M., Lubbers, J., Wieser, E., Ozaydin, S., Kent, A. & Till, C. 2022: Thermobar: An open-source Python3 tool for thermobarometry and hygrometry. Volcanica **5**(2), 349–384. *https://doi.org/10.30909/vol.05.02.349384*

Willigers, B.J.A., van Gool, J.A.M., Wijbrans, J.R., Krogstad, E.J. & Mezger, K. 2002: Posttectonic cooling of the Nagssugtoqidian Orogen and a comparison of contrasting cooling histories in precambrian and phanerozoic orogens. Journal of Geology **110**(5), 341595. *https://doi.org/10.1086/341595*

Wu, C.M., Zhang, J. & Ren, L.D. 2004: Empirical Garnet–Biotite–Plagioclase–Quartz (GBPQ) geobarometry in medium- to high-grade metapelites. Journal of Petrology **45**(9), 1907–1921. *https://doi.org/10.1093/petrology/egh038*